AAS/AIAA 25-298

MODELING AND NAVIGATION FILTERING FOR SPACECRAFT RENDEZVOUS WITH FLEXIBLE APPENDAGES AND SLOSHING

Thomas Claudet[*], Francesco Sanfedino[†], Paolo Panicucci[‡],
Damiana Losa[§], and Daniel Alazard[¶]

Flexibility is a fundamental aspect of very close proximity operations, for which its understanding shall allow faster, safer, and more precise operations in space. A chaser satellite is modeled using a Linear Fractional Representation (LFR), taking into account uncertainties in the relative translation and rotation between the chaser and the target, but also large flexible solar panels, a 6-link robotic arm with flexible joints, a 4-reaction-wheel system, a large flexible boom antenna and fuel sloshing. The model is then validated using Simscape Multibody. Then, integrating the flexible information, an LFR-based Kalman Filter is developed to precisely estimate chaser relative pose exploiting keypoints belonging to the target shape. These latter are identified by two cameras: one mounted on the main rigid hub, and the other one at the end-effector of the robotic arm. Numerical Monte-Carlo simulations and sensitivity analyses investigate the proposed approach for a typical in-orbit servicing scenario.

INTRODUCTION

With applications ranging from autonomous in-orbit servicing, assembly, and manufacturing to orbital debris removal, the complexity of rendezvous operations with space manipulator systems presents significant challenges in enhancing performance while ensuring safety.[1] To enable more agile operations, a key aspect is dealing with flexibility, specifically the deflection of mechanical structures under loads and their subsequent coupling with the Attitude & Orbit Control Subsystem (AOCS).[2] During very close proximity operations, because of the coupling between attitude and translation, applied forces and torques can significantly excite structural flexible modes, which may cause disturbances to the robotic arm's end-effector and potentially lead to collisions.[3] However, guidance and navigation models typically used in the AOCS are often simplified by using a rigid-body assumption, which does not adequately capture the dynamics of spacecraft with large flexible components (e.g.,, solar arrays, booms, robotic arms). This assumption becomes more and more obsolete with the development of space missions of the new generation involving very large structures (e.g., space power generators[4]), agile spacecrafts for exploration,[5] or rendezvous operations.[6,7] Therefore, on the navigation side, assuming a rigid model could lead to unacceptable errors (e.g., tens to hundreds of pixels) between the projection of key points identified by vision algorithms and the actual relative position and orientation between the two spacecraft. Understanding the impact of flexibility on spacecraft navigation in close proximity can thus be key to advance agile in-orbit servicing capabilities.

In this context, this paper aims at addressing a significant gap in the literature by taking into account uncertainties and varying parameters in a unique analytical linear model, which can be evaluated at each desired step of the navigation filter. A comprehensive modeling of complex multibody structures allows for

---

[*] Ph.D. Student, Fédération ENAC ISAE-SUPAERO ONERA, Université de Toulouse, 10 Avenue Marc Pélegrin, 31055 Toulouse, France. IRT Saint-Exupery, 3 Rue Tarfaya, 31400 Toulouse, France.

[†] Associate Professor, Fédération ENAC ISAE-SUPAERO ONERA, Université de Toulouse, 10 Avenue Marc Pélegrin, 31055 Toulouse, France.

[‡] Assistant Professor, Department of Aerospace Science and Technology (DAER), Politecnico di Milano, Via La Masa 34, 20156, Milan.

[§] Mission Analysis and GNC R&D Engineer, IRT Saint-Exupery, 3 Rue Tarfaya, 31400 Toulouse, France.

[¶] Professor, Fédération ENAC ISAE-SUPAERO ONERA, Université de Toulouse, 10 Avenue Marc Pélegrin, 31055 Toulouse, France.

early prediction of worst-case scenarios, thereby pushing the system to its performance limits and reducing design margins.

To help building fully parameterized models based on the system's geometrical configuration, the Two-Input Two-Output Ports (TITOP) approach[8] is used. The TITOP method allows for the modeling of complex multibody mechanical systems while maintaining the uncertain nature of the system and encapsulating all possible mechanical configurations in a single low-order Linear Fractional Representation (LFR). Models developed using the TITOP approach are well-suited for robust control synthesis,[9] but their possible extension to the estimation problem is also tackled in this paper. All TITOP-based models have been systematically integrated into the latest release of the Satellite Dynamics Toolbox library (SDTlib),[10] enabling users to easily build flexible spacecraft models with multiple appendages by assembling customized Simulink blocks.

This paper introduces the following key contributions:

- The development and validation of a comprehensive model that fully captures, in an LFR, the uncertain dynamics between the target spacecraft and the cameras mounted on the rigid hub and at the end-effector of the chaser's robotic arm. The model takes into account uncertainties in the relative translation and rotation between the chaser and the target, but also large flexible solar panels, a 6-link robotic arm, a 4-reaction-wheel system arranged in a pyramidal configuration, a large flexible boom antenna and fuel sloshing.
- The use of this model to design an LFR-based Kalman Filter in a realistic in-orbit scenario that accounts for all the possible configurations and couplings, including flexibility, between the different subsystems.

This paper is organized into three main sections. Firstly, a short illustrative study is presented in order to highlight the impact of flexibility in the navigation problem and motivate the interest of the proposed solution. Secondly, a linear parameter varying (LPV) model is sought using SDT, resulting in an LFR that minimizes parameter occurrences. The proposed model design is validated using a nonlinear physics simulator built with MathWorks' Simscape multibody toolset. Then, an LFR-based Kalman Filter is implemented to meet stringent performance requirements of 5 pixels maximum projection error within a realistic in-orbit scenario. Subsequent sensitivity analyses show the performance of the chosen approach and its performance with respect to measurement noise levels as well as correction time.

An illustrative video of the reference scenario can be found at `https://youtu.be/Qt1UK2N8ZrY`. Here, the chaser approaches the target and extends its robotic arm to reach the target's docking port.

FLEXIBILITY IMPACT QUANTIFICATION

To motivate the use of a navigation filter integrating flexible dynamics, it is important to quantify the impact of such often-neglected dynamical effects in a realistic rendezvous scenario. The models used in this comparison result from the ones described in their dedicated section thereafter. First, Figures 1 and 2 show the impact of flexibility as a difference in pixel coordinates for the projection of a feature point on the cameras described in Table 1. Only geometry in the projection was taken into account, with no other optical considerations. Position of the selected features for the study are shown on Figure 3.

Figure 1 highlights the differences in pixels between a rigid and a flexible model of the projection of the target feature points onto the camera attached to the end effector of the robotic arm. The left plots show the trajectories of selected features (P_x vs P_y) for both models and time is shown with an arrow under the letter t. The rigid model trajectories are depicted in black, while the flexible model trajectories are shown in red. It is observed that flexibility introduces substantial deviations, as reflected in the right column, which visualizes the error trajectories (ΔP_x vs ΔP_y).

In comparison, Figure 2 illustrates the same simulation but from the camera attached to the rigid body. While deviations between the rigid and flexible models are still visible, they are of lower frequencies, but one can clearly see the lag and lead behavior introduced by the bending of the structures and the sloshing particles bouncing to the side of the tank. The error trajectories in the right plots confirm again that the discrepancies are rapidly growing. Although being highly dependent on the image processing, for tasks involving high precision, such as robotic arms handling delicate operations or spacecraft docking, projection errors exceeding 5 pixels are generally considered unacceptable. These observations motivate the need for incorporating flexibility into a dedicated navigation filter.

Table 1. Camera intrinsic parameters

Focal Length (mm)	50	Number of pixels (px)	1024	Size of CCD sensor (mm)	36
Principal point (px)	(0, 0)	Skew parameter	0	Lens distortion	0

MULTIBODY MODELING

This section presents a comprehensive multibody modeling framework designed to capture the dynamic interactions between the spacecraft's rigid hub and its flexible appendages based on previous work.[11,12] Using the Two-Input Two-Output Port (TITOP) method, the flexible appendages are modeled in a modular fashion, allowing the system's dynamic equations to be systematically derived and parameterized. The resulting Linear Fractional Representation (LFR) integrates uncertainties, such as joint flexibility, structural modes, and sloshing dynamics, providing a compact and efficient representation for control and filtering tasks.

The framework also incorporates contributions from the reaction wheel system and robotic arm, which introduce additional coupling effects. The developed model is validated against a nonlinear Simscape simulation, confirming its ability to represent the dynamics of the system under a broad range of operating conditions. A general schematic of the situation is found in Figure 3, where the physical layout of the system is depicted. The target satellite ($\mathcal{T}$) is approached by the chaser spacecraft ($\mathcal{C}$), which consists of a rigid hub ($\mathcal{RH}$), two large flexible solar arrays ($\mathcal{SA}_1$ and $\mathcal{SA}_2$), a large flexible boom antenna ($\mathcal{A}$), a robotic arm ($\mathcal{RA}$), and sloshing dynamics represented by ($\mathcal{S}$). A pyramid of reaction wheels ($\mathcal{RW}$) is used for torque control. The key feature points (G_{t_i}) of the target satellite are observed by two cameras: one fixed to the rigid hub ($\mathcal{C}_1$) and another mounted on the end effector of the robotic arm ($\mathcal{C}_2$).

The TIPOP Approach

For each subsystem (rigid body, solar arrays, antenna, arm joints and links, reaction wheels, sloshing), the TITOP model links the dynamics between boundary wrenches (forces/torques) and accelerations (linear and angular), giving 12 inputs and 12 outputs (see Figure 4 for a graphical representation):

- The 6 input components of the Wrench $\left[\boldsymbol{W}_{\mathcal{L}_{i+1}/\mathcal{L}_i,C_i}\right]_{\mathcal{R}_i} = \begin{bmatrix}\boldsymbol{F}_{\mathcal{L}_{i+1}/\mathcal{L}_i} \\ \boldsymbol{T}_{\mathcal{L}_{i+1}/\mathcal{L}_i,C_i}\end{bmatrix}_{\mathcal{R}_i}$ applied by the substructure $\mathcal{L}_{i+1}$ to $\mathcal{L}_i$ at point C_i. It is expressed in frame $\mathcal{R}_i = (P_i^0; x_i, y_i, z_i)$ about P_i^0, namely point P_i in the undeformed configuration, and x_i, y_i, z_i the attached basis.
- The 6 input components of the acceleration twist $\left[\ddot{\boldsymbol{x}}_{P_i}\right] = \begin{bmatrix}\boldsymbol{a}_{P_i} \\ \dot{\boldsymbol{\omega}}_{P_i}\end{bmatrix}_{\mathcal{R}_i}$,
- The 6 output components of the acceleration twist $\left[\ddot{\boldsymbol{x}}_{C_i}\right] = \begin{bmatrix}\boldsymbol{a}_{C_i} \\ \dot{\boldsymbol{\omega}}_{C_i}\end{bmatrix}_{\mathcal{R}_i}$,
- The 6 output components of the Wrench $\left[\boldsymbol{W}_{\mathcal{L}_i/\mathcal{L}_{i-1},P_i}\right] = \begin{bmatrix}\boldsymbol{F}_{\mathcal{L}_i/\mathcal{L}_{i-1}} \\ \boldsymbol{T}_{\mathcal{L}_i/\mathcal{L}_{i-1},P_i}\end{bmatrix}_{\mathcal{R}_i}$ applied by the substructure $\mathcal{L}_i$ to $\mathcal{L}_{i-1}$ at point P_i.

To provide a comprehensive understanding of the spacecraft's dynamics, the following paragraphs detail the TITOP modeling of each subsystem, including the rigid hub, flexible appendages, reaction wheels, sloshing dynamics, and the robotic arm, along with their integration into the overall multibody framework.

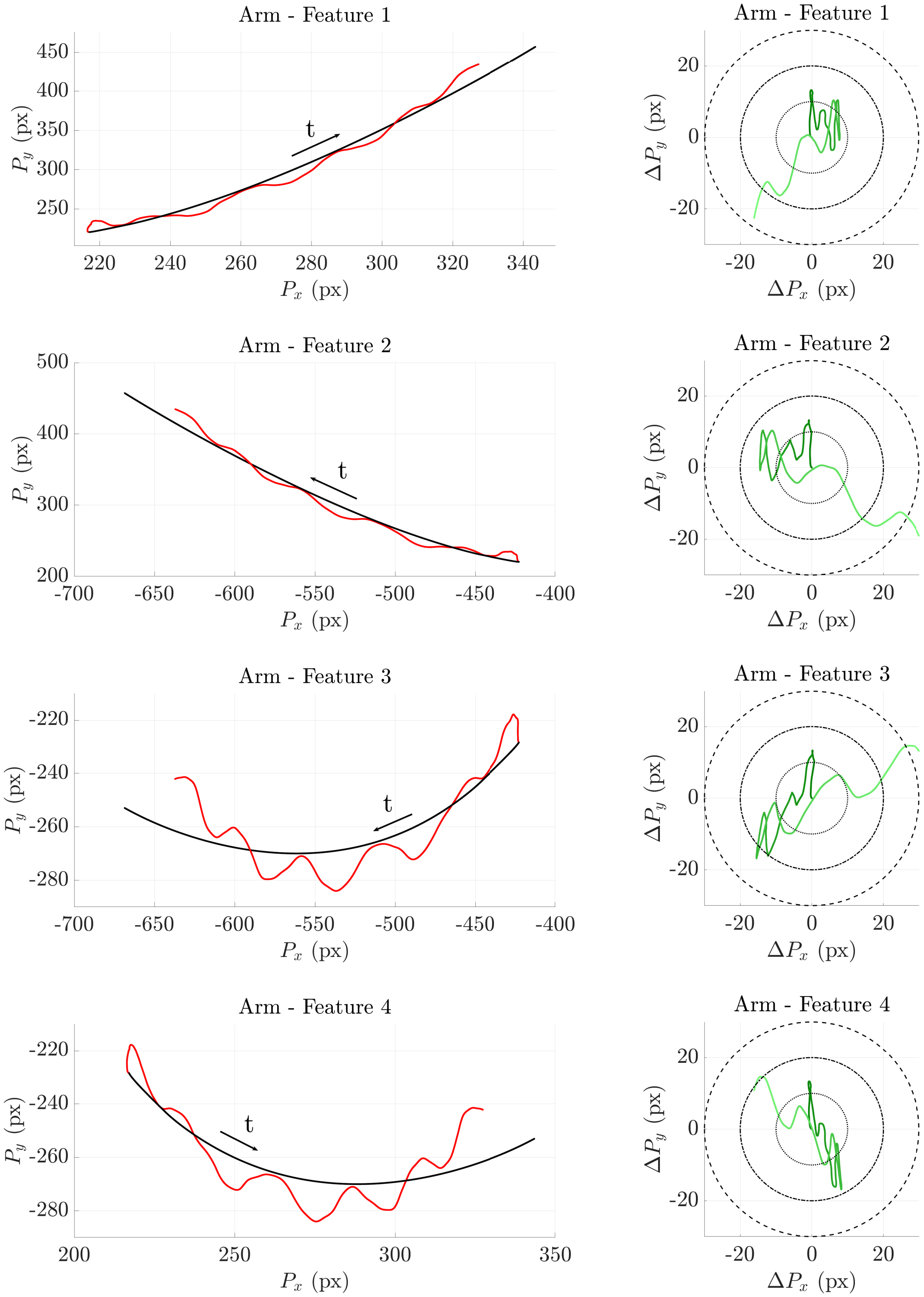

Figure 1. Projection of the features on the arm camera in pixels between the rigid model (black) and the flexible one (red) from the very beginning of the approach. Both models have the same initial conditions, therefore showing zero initial pixel projection errors. The center of the image has (0,0) coordinates. As time increases, the error goes from dark to light green.

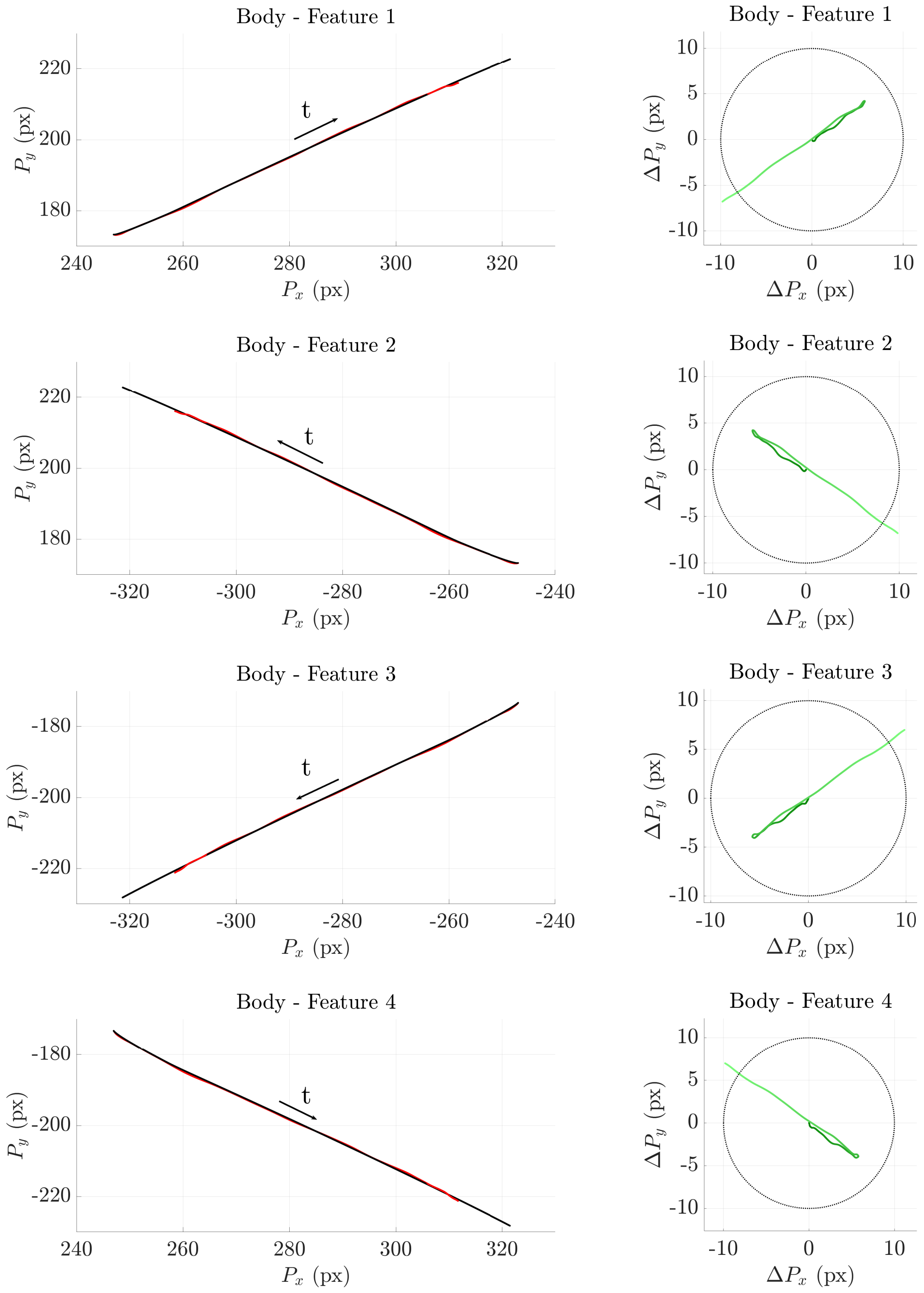

Figure 2. Projection of the features on the body camera in pixels between the rigid model (black) and the flexible one (red) from the very beginning of the approach. Both models have the same initial conditions, therefore showing zero initial pixel projection errors. The center of the image has (0,0) coordinates. As time increases, the error goes from dark to light green.

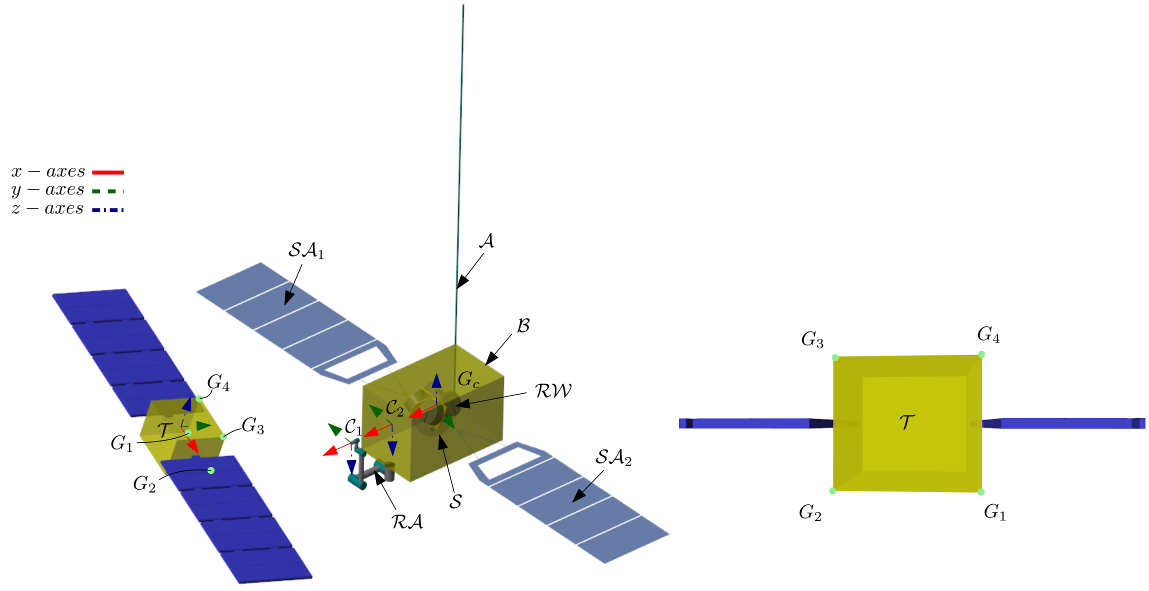

(a) (b)

Figure 3. (a) General view of the target $\mathcal{T}$ and the chaser $\mathcal{C}$ with its rigid hub $\mathcal{RH}$, two large flexible solar arrays $\mathcal{SA}_1$ and $\mathcal{SA}_2$, the large flexible boom antenna $\mathcal{A}$, its reaction wheels pyramid $\mathcal{RW}$, sloshing in the fuel tank $\mathcal{S}$ and a robotic arm $\mathcal{RA}$. The feature points on the target G_{t_i} are seen from the cameras positioned on the rigid hub $\mathcal{C}_1$ and at the end-effector $\mathcal{C}_2$. (b) View form the end-effector camera in the recorded scenario, where the position of the four feature points are highlighted.

Main Rigid Hub

The main rigid body $\mathcal{B}$ of the chaser with center of mass B is assumed rigid and its dynamics in an inertial frame are directly given by Newton-Euler's equation:

$$\begin{bmatrix} \boldsymbol{F}_{ext} \\ \boldsymbol{T}_{ext,B} \end{bmatrix} = \underbrace{\begin{bmatrix} m^{\mathcal{B}}\boldsymbol{I}_3 & \mathbf{0}_{3\times3} \\ \mathbf{0}_{3\times3} & \boldsymbol{I}_B^{\mathcal{B}} \end{bmatrix}}_{\boldsymbol{D}_B^{\mathcal{B}}} \begin{bmatrix} \boldsymbol{a}_B \\ \dot{\boldsymbol{\omega}} \end{bmatrix} + \begin{bmatrix} \mathbf{0}_{3\times3} \\ \boldsymbol{\omega} \wedge \boldsymbol{I}_B^{\mathcal{B}}\boldsymbol{\omega} \end{bmatrix}, \tag{1}$$

with $\boldsymbol{D}_B^{\mathcal{B}}$ the static/rigid dynamics model. The angular velocity $\boldsymbol{\omega}$ is actively controlled around zero with respect to the target reference frame, itself assumed non-rotating. The second term is therefore neglected and the equation becomes linear.

Flexible Solar Panels and Antenna

While the antenna was represented as a flexible beam in this work, solar panels are modeled by complex Finite Element Method (FEM) meshes, in which panels are modeled using plate elements to capture their flexibility and vibrational characteristics. Yokes that connect the solar panels to the spacecraft body and provide support and rotation mechanisms are modeled using beam elements to handle their slender geometry and support functions. Finally, junctions between the panels and yokes are modeled with Multipoint Constraints (MPCs) to ensure the structural integrity and proper mechanical interaction. First designed on specialized finite element softwares like Patran/Nastran, their direct dynamics model is given in the frequency domain by:

$$\boldsymbol{M}_P^{\mathcal{A}}(s) = \boldsymbol{D}_P^{\mathcal{A}} - \sum_{i=1}^{N} \boldsymbol{l}_{i,P}^T \boldsymbol{l}_{i,P} \frac{s^2}{s^2 + 2\xi_i\omega_i s + \omega_i^2}, \tag{2}$$

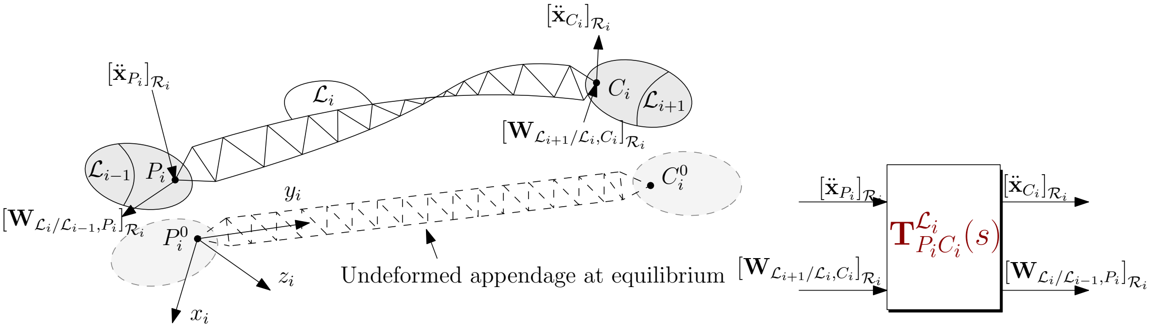

(a) (b)

Figure 4. (a) i-th flexible appendage of a body. (b) TITOP model of the appendage.

with $\boldsymbol{M}_P^{\mathcal{A}}$ the direct dynamics flexible model of the appendage $\mathcal{A}$ about the center of mass P, considering N modes of damping ratio ξ_i and natural frequency ω_i when $\boldsymbol{l}_{i,P}$ is defined as the i-th flexible mode's vector of modal participations expressed at point P in the frame $\mathcal{R}_a$. All of these values are directly retrieved from the software. $\boldsymbol{D}_P^{\mathcal{A}}$ is the 6×6 mass/inertia matrix of the appendage.

Figure 5 shows a meshed representation of the flexible solar array, created using Nastran/Patran software. The mesh captures the structural configuration and details required for finite element analysis to model its dynamic and flexible properties accurately. This meshed model serves as the foundation for deriving the modal parameters, such as natural frequencies and mode shapes, which are critical inputs for the dynamic modeling and simulation of the spacecraft's flexible components.

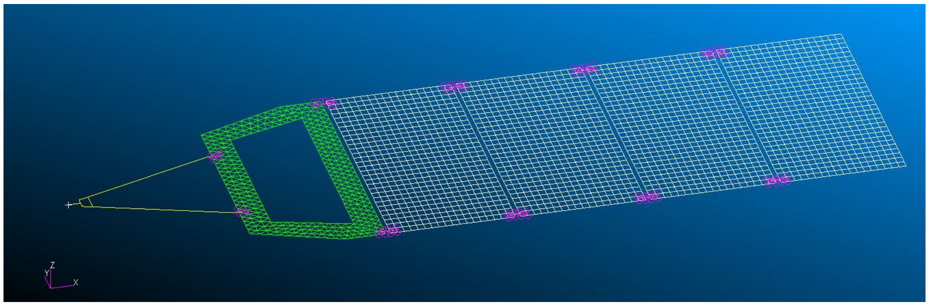

Figure 5. Screenshot from Nastran/Patran of the meshed flexible solar array. The yoke is in green, panels in white, and MPCs in pink.

Reaction Wheels

Torque control is achieved using a pyramid of reaction wheels. Their direct dynamics model is obtained from:

$$\boldsymbol{M}_P^{\mathcal{A}}(s) = \boldsymbol{D}_P^{\mathcal{A}} + \begin{bmatrix} \mathbf{0}_{3\times3} & \mathbf{0}_{3\times3} \\ \mathbf{0}_{3\times3} & -\frac{1}{s} I_w \Omega (^*\boldsymbol{z_w}) \end{bmatrix}, \tag{3}$$

with I_w the wheel inertia about its spin axis unit vector $\boldsymbol{z_w}$, Ω the spinning rate and $(^*\boldsymbol{z_w})$ is the anti-symmetric matrix associated with $\boldsymbol{z_w}$.

Fuel Sloshing

Sloshing is modeled by several particles, each connected to 3 perpendicular 1D spring-damper systems.[13] The equations are given by:

$$\begin{cases} m_{\mathcal{S}} \boldsymbol{I}_3 (\boldsymbol{a}_C + \delta \ddot{\boldsymbol{r}}_{\mathcal{S}}) = -k_{\mathcal{S}} \boldsymbol{I}_3 \delta \boldsymbol{r}_{\mathcal{S}} - c_{\mathcal{S}} \boldsymbol{I}_3 \delta \dot{\boldsymbol{r}}_{\mathcal{S}} \\ \boldsymbol{F}_{\mathcal{S}/\mathcal{B},C} = k_{\mathcal{S}} \boldsymbol{I}_3 \delta \boldsymbol{r}_{\mathcal{S}} + c_{\mathcal{S}} \boldsymbol{I}_3 \delta \dot{\boldsymbol{r}}_{\mathcal{S}} \end{cases}, \tag{4}$$

with $m_{\mathcal{S}}, k_{\mathcal{S}}, c_{\mathcal{S}}$, the mass of the fuel particle, spring stiffness and damping coefficient. Also, $\delta \boldsymbol{r}_{\mathcal{S}}$ is the displacement of the particle with respect to its equilibrium position. The acceleration of the connection with the parent body (tank and non-sloshing fuel mass) are given by $\boldsymbol{a}_C$ and the forces applied by the sloshing mass to the parent body $\boldsymbol{F}_{\mathcal{S}/\mathcal{B},C}$.

Robotic Arm with Flexible Joints

A robotic arm with 6 revolute joints (see Figure 6) is attached to the hub. Its characteristics are chosen to model the Universal Robot's UR5.[14]

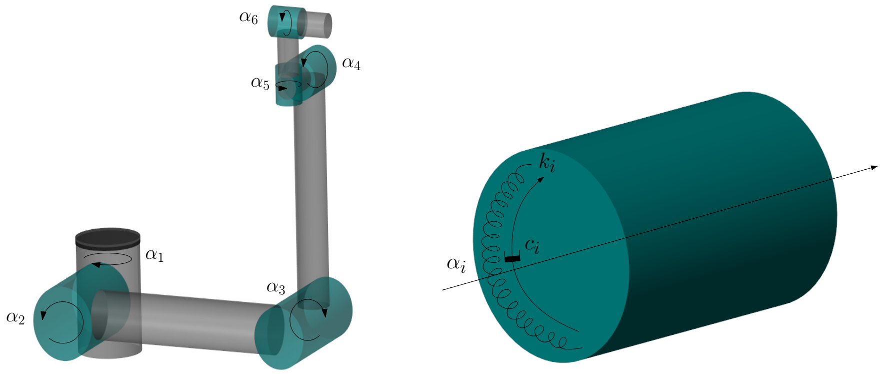

Figure 6. The 6-DOF robotic arm, parametrized by uncertain angles α_i (left). Torsional spring-damper system on every joint to model flexibility (right).

For space manipulator systems, it is reasonable to concentrate the flexibility lumped to the robot's joints, when dealing with short links.[3] Therefore, a torsional spring-damper system of stiffness k_i and damping ratio c_i is included into each link to model the arm flexible motion.

Linear Fractional Representation

Linear Fractional Representation (LFR) is a powerful mathematical framework widely used in control theory and dynamical modeling to represent systems with parametric uncertainties. The LFR formalism expresses a dynamic system as a structured interconnection of a nominal system and a perturbation matrix $\boldsymbol{\Delta}$, that captures uncertainty and variability in parameters.[15] This approach allows complex systems, such as flexible spacecraft with appendages, to be efficiently represented while retaining essential dynamics and uncertain behaviors.[16] In the context of spacecraft rendezvous, the LFR model encapsulates the relationship between inputs (forces, torques), and outputs (the relative pose of the target with respect to the cameras), accounting for the position of the arm in terms of uncertain angles as well as the dynamic interactions caused by flexible components and sloshing. By providing a compact, yet comprehensive representation, LFR facilitates real-time computation and robust analysis, making it particularly suitable for navigation filtering and control design tasks under changing and uncertain operational conditions.

Figure 7 provides a schematic representation of the spacecraft system and its LFR model to capture dynamic interactions and uncertainties. The LFR captures the dynamic relationships between external forces and torques ($\boldsymbol{F}_{ext}, \boldsymbol{T}_{ext}$), the joint torques ($\boldsymbol{T}_{q_{arm}}$), the reaction wheels' control torques ($\boldsymbol{T}_{RW}$), and the flexible components of the system. The green block represents the structured uncertainty, including parametric variations of:

- $\boldsymbol{\Delta r}_{ct} = \text{diag}\left(\Delta x_{ct}, \Delta y_{ct}, \Delta z_{ct}\right)$, the relative positions uncertainties of x_{ct}, y_{ct}, z_{ct} in the target frame,
- $\boldsymbol{\Delta\Theta}_{ct} = \text{diag}\left(\Delta\varphi_{ct}, \Delta\theta_{ct}, \Delta\psi_{ct}\right)$, the relative Euler angle uncertainties,

- $\boldsymbol{\Delta q}_{arm} = \mathrm{diag}\left(\Delta q_1, \Delta q_2, \Delta q_3, \Delta q_4, \Delta q_5, \Delta q_6\right)$, the 6 robotic arm joint angle uncertainties.

The nominal model ($\mathcal{P}$) allows one to compute the relative pose between the target and the cameras ($\mathcal{C}_1/\mathcal{T}$) and ($\mathcal{C}_2/\mathcal{T}$), but also the relative angular velocity $\boldsymbol{\omega}_{ct}$ as well as the joint angles $\boldsymbol{q}_{arm}$ This LFR-based representation enables efficient encapsulation of the parametric uncertainties and is directly provided to the navigation filter design.

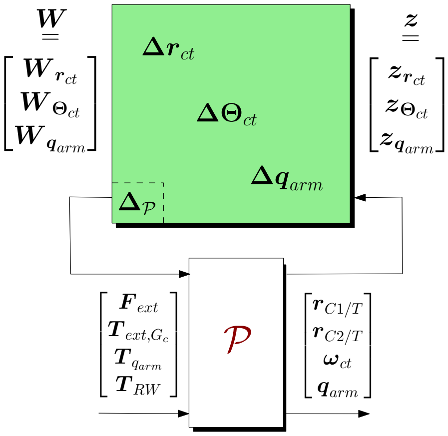

Figure 7. The Linear Fractional Representation of the transfer between the forces/torques and the relative pose from the feature point to the camera pose at the end-effector with all the parametric uncertainties. $\boldsymbol{W}$ represents the external inputs, and $\boldsymbol{z}$ the external outputs.

Relative Frame and Nonlinear Angular Integration

Generally TITOP models all refer to the body frame of each sub-structure. Here the positions of the cameras need to be expressed with respect to the target frame. Rotation matrices following the ZYX sequence are then added to account for it. They are parametrized with respect to each uncertain angle[17] leading to a minimal LFR representation.

Moreover, in order to better match the outputs of the nonlinear high fidelity model for the attitude, angular velocities are not simply integrated, but the nonlinear expression[18] is being used as a block outside of the linear model:

$$\begin{bmatrix} \dot{\varphi} \\ \dot{\theta} \\ \dot{\psi} \end{bmatrix} = \frac{1}{\cos\theta} \begin{bmatrix} \cos\theta & \sin\varphi\sin\theta & \cos\varphi\sin\theta \\ 0 & \cos\varphi\cos\theta & -\sin\varphi\cos\theta \\ 0 & \sin\varphi & \cos\varphi \end{bmatrix} \begin{bmatrix} p \\ q \\ r \end{bmatrix}, \tag{5}$$

with p, q, r the components of the angular velocity vector. Special handling (e.g., with quaternions) could be used in singular cases.

Simscape Validation

In order to validate the model linearized using the SDT library, a non-linear high-fidelity simulator is built in parallel using Mathworks' Simscape Multibody library. Then, its automatic linearization allows to compare between the two models in the entire frequency domain, as shown in Figure 8. One key point is that for the filtering, this Simscape model is not directly used because the derived LPV model build aside contains by construction all the possible system configurations encapsulated in just one single model. This would not be possible using Simscape, since a computationally intensive linearization step would be necessary in the estimation process every time the model would have to be updated.

The transfer shown is from the:

- force/torque inputs at the center of mass of the chaser,
- the joint individual torques,
- the torque given to the reaction wheels,

to the relative positions of the target frame with respect to each camera frame, projected into the target frame. Figure 8 presents the nominal singular value responses for both models, along with the sampled differences obtained from 100 randomized parameter configurations (following the uncertainty represented in Figure 7). The frequency response spans from 10^{-2} rad/s to 10^4 rad/s, covering all the flexible modes of the system.

The nominal responses from SDTlib (red) and Simscape (blue) align closely across all frequencies, indicating the accuracy of the SDTlib model in capturing the system's linear dynamics. The green dotted lines, representing the sampled differences, are in the order of -400dB to -75dB evolving during the mission scenario, validating the robustness of the LFR model in accounting for parametric uncertainties and dynamic couplings. This ensures that the model is well-suited for use in the navigation filtering section, where precise representation of the system dynamics is crucial. Note that this validation was performed in the frequency domain, but a dedicated validation in the time domain was performed and it is not reported here for the sake of brevity.

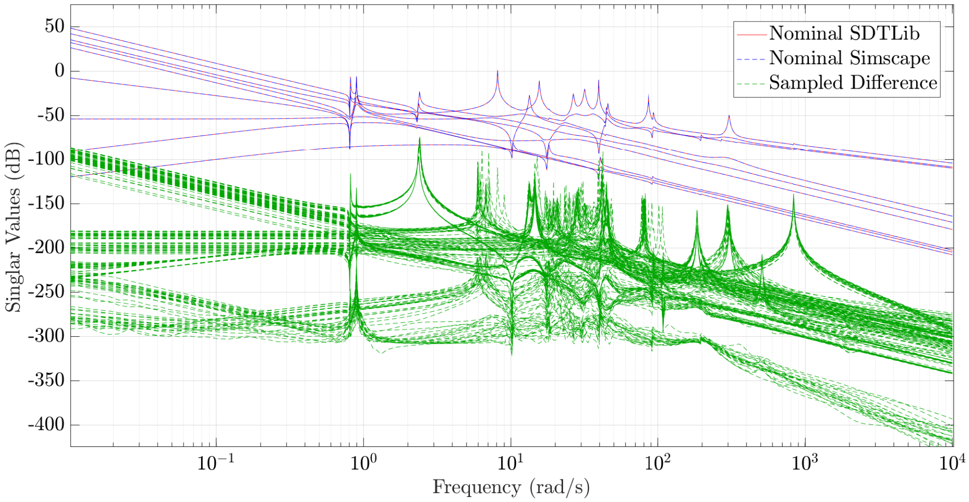

Figure 8. Comparison between SDTlib and Simscape in the nominal configuration and sampled difference over 100 runs with randomized parameters, validating the model to be used in the navigation section.

NAVIGATION FILTER

LFR-based Kalman Filtering

An LFR-based Kalman Filter is developed to accommodate the hybrid dynamics of flexible spacecraft systems. The algorithm operates in two main stages: prediction and correction, combining the strengths of continuous state propagation and discrete measurement updates. The filter is processing the relative positions of the cameras, which makes the approach a loosely coupled one (e.g., data from the cameras are processed independently to estimate state variables). This makes sense for applications with fewer computational resources even though a tightly coupled scheme would increase precision, but at the cost of more processing effort.

Prediction In the prediction step, the state and covariance are propagated forward in time using the system's dynamics. The state propagation is performed using the LFR-based system matrices. Directly working with this LFR model is advantageous since one only needs to evaluate it according to the current values of the varying parameters. The system dynamics are described by the equation:

$$\dot{\mathbf{x}}(t) = \mathbf{A}(\boldsymbol{\Delta})\mathbf{x}(t) + \mathbf{B}(\boldsymbol{\Delta})\mathbf{u}(t), \tag{6}$$

where $\mathbf{x}(t)$ represents the state vector at time t, $\mathbf{A}(\boldsymbol{\Delta})$ is the state transition matrix, function of the uncertain parameters, $\mathbf{B}(\boldsymbol{\Delta})$ the input matrix, and $\mathbf{u}(t)$ the input vector at time t (composed of the external wrench, joint and wheels torques). All the states were propagated, but further studies on a reduced order model could be beneficial to save computational resource.

The covariance matrix evolves over time according to the following differential equation:

$$\frac{d\mathbf{P}(t)}{dt} = \mathbf{A}(\boldsymbol{\Delta})\mathbf{P}(t) + \mathbf{P}(t)\mathbf{A}^{\top}(\boldsymbol{\Delta}) + \mathbf{Q}. \tag{7}$$

Here, $\mathbf{P}(t)$ is the state covariance matrix, and $\mathbf{Q}$ represents the process noise covariance.

Correction The correction step occurs when measurements are received. At this point, the predicted state and covariance are updated based on the new information provided by the measurements. The innovation, which is the difference between the actual measurement and the predicted measurement, is computed as:

$$\mathbf{y}_k = \mathbf{z}_k - \mathbf{H}(\boldsymbol{\Delta})\mathbf{x}_k, \tag{8}$$

where $\mathbf{z}_k$ represents the measurement vector, and $\mathbf{H}(\boldsymbol{\Delta})$ is the observation matrix that maps the state to the measurement space.

The Kalman gain, which determines how much the state estimate should be adjusted based on the new measurement, is calculated as:

$$\mathbf{K}_k = \mathbf{P}_k^{-}\mathbf{H}^{\top}(\boldsymbol{\Delta})\left(\mathbf{H}(\boldsymbol{\Delta})\mathbf{P}_k^{-}\mathbf{H}^{\top}(\boldsymbol{\Delta}) + \mathbf{R}\right)^{-1}, \tag{9}$$

where $\mathbf{P}_k^{-}$ is the predicted covariance matrix, and $\mathbf{R}$ is the measurement noise covariance.

Using the innovation and the Kalman gain, the state and covariance are updated. The updated state is given by:

$$\mathbf{x}_k^{+} = \mathbf{x}_k^{-} + \mathbf{K}_k\mathbf{y}_k, \tag{10}$$

and the updated covariance is:

$$\mathbf{P}_k^{+} = \mathbf{P}_k^{-} - \mathbf{K}_k\mathbf{H}(\boldsymbol{\Delta})\mathbf{P}_k^{-}. \tag{11}$$

In this step, $\mathbf{x}_k^{+}$ and $\mathbf{P}_k^{+}$ represent the corrected state and covariance matrices, respectively. This correction ensures that the state estimate is refined using the information from the new measurement.

Leveraging the LFR formalism, the algorithm speeds-up computations by dynamically evaluating the state-space matrices based on measurements only when a certain threshold is exceeded (e.g., the arm joint angles or the satellite's attitude were slightly changed with respect to the previous evaluation). Of course, updating the model at each time would increase the precision, but it was found that this made the computations faster for a similar precision, which can be seen as model robustness. The state propagation happens in continuous time with the linearized model, while the correction step occurs at discrete intervals when measurements are received.

This correction steps allows to recover the mismatch between the LPV model and the nonlinear high-fidelity simulator thanks to the measurements. In practice, the LPV model is used for the propagation, which consists in the evaluation of the LFR. At this stage, this evaluation is done with the *usubs* Matlab function.

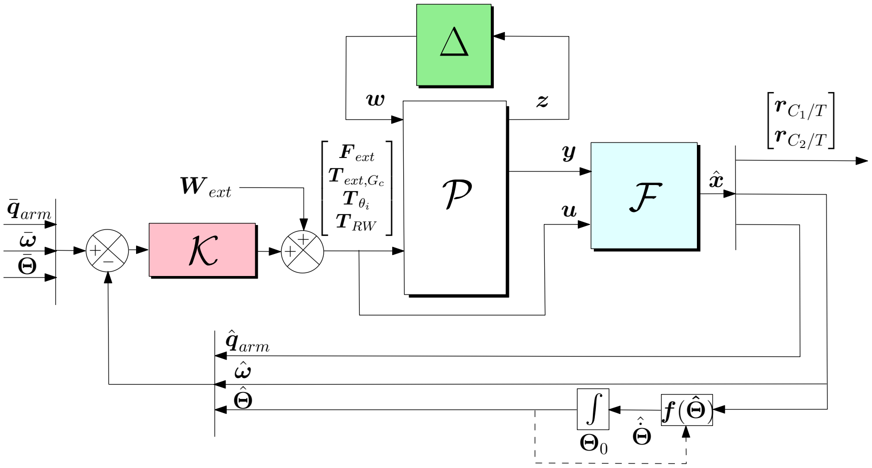

Figure 9. Closed loop schematic

A computationally efficient evaluation of this model is a subject not covered in this paper and needs further research for practical implementation.

The closed-loop schematic of the system is provided in Figure 9. The controller ($\mathcal{K}$) generates control commands based on the system estimated states ($\hat{\boldsymbol{q}}_{arm}, \hat{\boldsymbol{\omega}}, \hat{\boldsymbol{\Theta}}$) and desired trajectories ($\bar{\boldsymbol{q}}_{arm}, \bar{\boldsymbol{\omega}}, \bar{\boldsymbol{\Theta}}$). The plant ($\mathcal{P}$) with its uncertainty block ($\boldsymbol{\Delta}$) represent the physical system being controlled. The filter ($\mathcal{F}$) estimates the state to provide accurate feedback for control. $\boldsymbol{W}_{ext}$ represents external control signals (e.g., thrust impulses to move the satellite). $\boldsymbol{f}(\hat{\boldsymbol{\Theta}})$ is the nonlinear equation given by Eq. (5), computing the time derivative of the Euler angles $\dot{\hat{\boldsymbol{\Theta}}}$, while $\boldsymbol{\Theta}_0$ is the initial angular configuration for the integration. $\boldsymbol{y}$ depicts the measurements, $\boldsymbol{u}$ the controls, $\hat{\boldsymbol{x}}$ the estimated states, $\boldsymbol{w}$ the external inputs, and $\boldsymbol{z}$ the external outputs. $\boldsymbol{r}_{C_i/T}$ the position vector of camera $\mathcal{C}_i$.

Filter Tuning

In the Kalman filter, the matrices $\mathbf{P}$, $\mathbf{Q}$, and $\mathbf{R}$ represent key aspects to handle uncertainty in the system. The matrix $\mathbf{P}$ is the state covariance, quantifying the uncertainty in the estimated state. The matrix $\mathbf{Q}$ is the process noise covariance, capturing model uncertainties and disturbances, influencing how $\mathbf{P}$ grows during prediction. Finally, $\mathbf{R}$ is the measurement noise covariance, characterizing sensor uncertainties and determining the trust placed on measurements during the correction step. Together, these matrices balance the contributions of the model and measurements for accurate state estimation.

In this work, assuming synchronization with the target movement, an initial uncertainty on the relative pose was set to 1 cm along the 3 axes, and the initial relative angular velocity of the chaser to 0.01 rad/s (about 0.5 deg/s) about the 3 axes. The uncertainty on the dynamics were attributed to the relative 6-DOF velocities as well as the joint angular velocities, to the extent of 10^{-4} in their relative units. Finally, the measurement matrix was set to $\boldsymbol{R} = A_{noise}^2 \boldsymbol{I}_6$, with the noise amplitude on the measurements $A_{noise} = 1$ cm.

Monte-Carlo Simulations

To further validate the model, a Monte Carlo (MC) campaign was performed by simulating the scenario 100 times with different initial conditions where the initial estimated states were randomly sampled from a Gaussian distribution around their nominal values, scaled by a factor $\sqrt{\mathrm{diag}(\boldsymbol{P})}$. Again, the first part of the scenario is a straight translation towards the target with deceleration in the last part, which provokes an oscillation of the panels, the antenna beams, and the sloshing particles, exhibiting their respective bending modes. Then, the arm extends following a predefined trajectory which excites its faster modes.

Figure 10 shows the Monte-Carlo position errors (gray lines) and their associated 3σ covariance bounds (red lines) for both the relative positions of the cameras on the arm end-effector and rigid hub components with respect to the target, projected in the target's X, Y, and Z base axes. The errors represent the difference between the true positions and the estimated positions produced by the Kalman filter.

The left column corresponds to the estimation error of the end-effector states, where the position errors initially exhibit variability before converging within the 3σ bounds as the filter stabilizes. This behavior reflects the influence of flexibility dynamics, particularly along the X and Z axes, where the flexibility is most pronounced as the arm extends in these directions.

The right column displays the position errors for the rigid hub-attached camera, which show faster convergence and remain tightly bound within the 3σ limits throughout the simulation. This indicates a more stable and predictable system behavior for the rigid body components, indeed the flexible modes being slower.

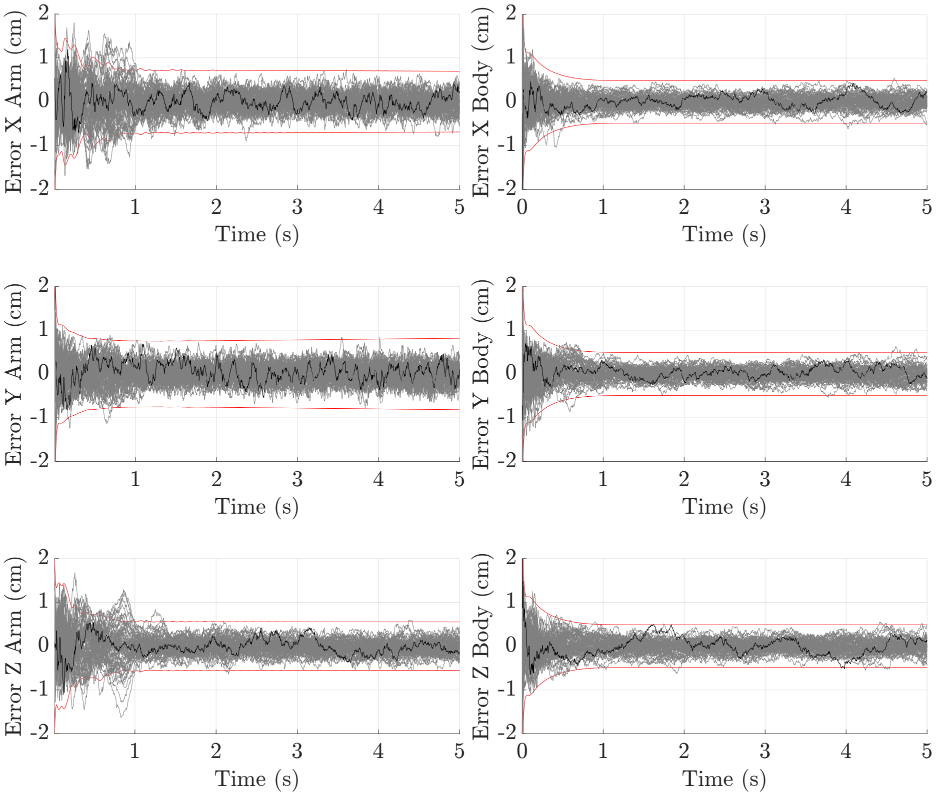

Figure 10. Position errors and 3σ covariance bounds. The gray traces represent the position errors, while the red lines indicate the 3σ covariance bounds. Black lines represent randomly-picked samples.

Probability Density Functions and Post-Fit Residuals

Figure 11 presents the PDFs of the estimation error for the arm and body components along the X, Y, and Z axes after convergence of the filter. The purple distributions represent the PDFs of the estimation error obtained from the Kalman filter, while the orange distributions correspond to the measurement noise. This plot is only possible because the measurement is the state.

The left column illustrates the end-effector position estimation errors while the right column shows the rigid body's ones. Slightly larger distributions are observed for the arm due to the additional dynamic disturbances caused by the manipulator's flexibility.

The comparison between the estimation error and the noise highlights the performance of the Kalman filter in maintaining error distributions within acceptable bounds, noting that there is a perfect image processing where measurements are directly taken from the model and noise is added on top. This alignment reflects the filter's ability to effectively reject noise and produce accurate estimates.

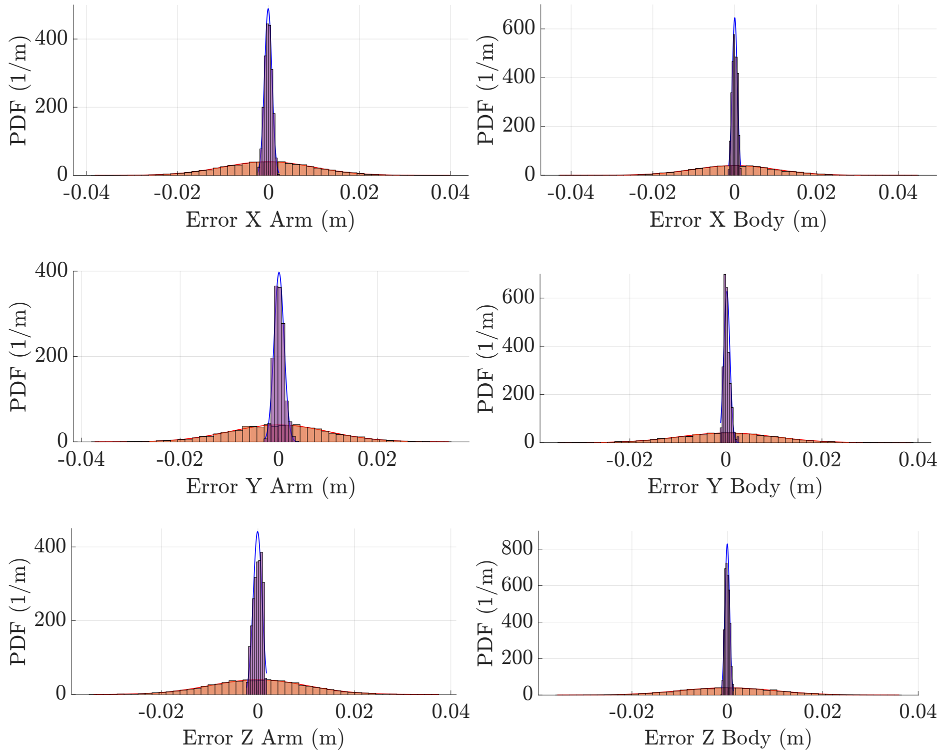

Figure 11. Probability density functions in the estimation error (purple) with respect to the noise (orange). The comparison highlights the ability of the Kalman filter to reject noise and maintain error distributions tightly aligned with the measurement noise.

Figure 12 illustrates the Post-Fit Residuals (PFR) for both the arm end-effector and rigid hub cameras components along the X, Y, and Z axes of the target frame after convergence of the filter. The PFR represents the difference between the observed measurements and the predicted measurements after the Kalman filter update (estimated states converted into the measurement space). The histograms show the distribution of the PFR values with its associated red Gaussian fitting curve, while the blue curve represents the Gaussian measurement noise distribution. The alignment of the PFR distributions with the measurement noise curves indicates effective tuning and filtering of the Kalman filter, with the residuals being zero-mean and well within the expected bounds.

Sensitivity Analyses

In order to gain insight on the sensitivity of certain parameters on the filtering performance, a parametric study was performed. Figure 13 illustrates the position errors and 3σ covariance bounds, overlaying the MC simulations of Figure 10 with varying correction times for both the camera on the arm end-effector (left column) and on the rigid hub (right column) along the X, Y, and Z axes of the target body frame.

As the correction time decreases, the position errors and covariance bounds converge more tightly, reflecting the increased confidence in the state estimates provided by the filter. The arm components, particularly along the Z-axis, exhibit larger variability with larger correction time, highlighting the greater impact of flexibility on the estimation process. In contrast, the body components converge more rapidly and remain tightly bounded even with fewer steps, demonstrating their stability.

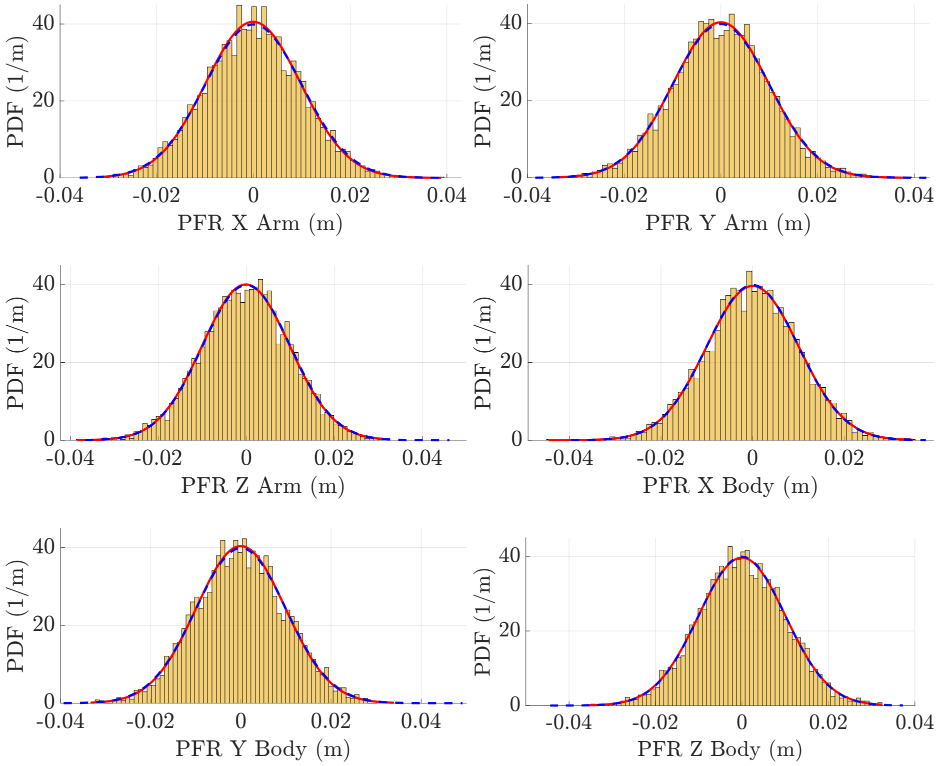

Figure 12. Post-Fit Residuals (PFR) (red) and measurement noise (blue). Effective tuning of the filter is checked from the zero-mean PFR and the superimposition with the measurement noise distribution.

The image processing (IP) frequency is a key aspect of the filtering performance. A value of 0.1s (orange), which could be an achievable performance with current IP and hardware, would therefore obtain almost the same performance as the best tested case shown in red. These results validate the importance of small correction times for achieving precise and consistent state estimation, especially for flexible components like the arm.

Then, Figure 14 illustrates the position errors and 3σ covariance bounds with varying levels of measurement noise for both the camera on the arm end-effector (left column) and rigid hub (right column) along the X, Y, and Z axes.

The figure demonstrates the importance of the measures for precise estimation of the arm. As the measurement noise increases (from red to green), the covariance bounds expand, reflecting reduced confidence in the state estimates. Despite the increased noise, the position errors (gray lines) remain well-contained within the 3σ bounds, validating the robustness of the Kalman filter in handling varying noise levels.

The arm components exhibit larger sensitivity to measurement noise, particularly along the Z-axis, where the covariance bounds expand more significantly. In contrast, the body components maintain tighter bounds, indicating greater stability and reduced noise sensitivity. These results underscore the importance of accurately modeling measurement noise to maintain precise and reliable state estimation.

Post-Filtering Camera Projections

Figures 15 and 16 illustrate the projection of key target features onto the camera arm and body frames throughout the entire scenario, with the center of the image corresponding to $(0, 0)$ coordinates. The left plot of each row indicates the feature trajectories (P_x vs P_y) before and after filtering, where the red line

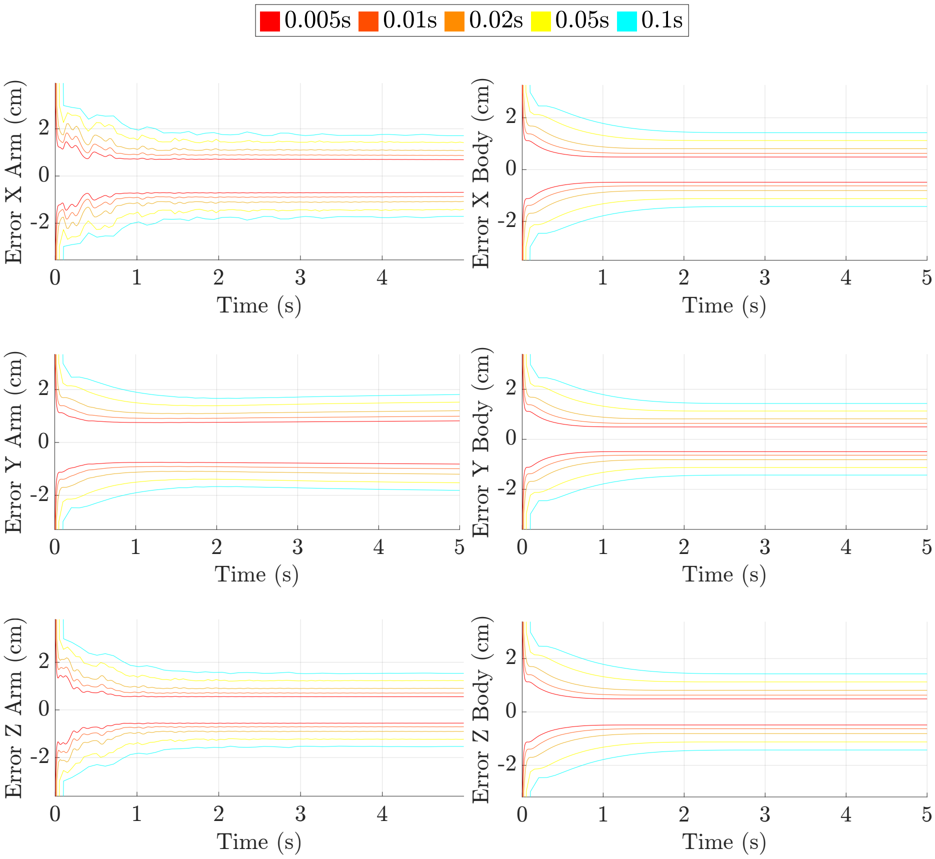

Figure 13. Position errors and 3σ covariance bounds with varying number of steps. The figure highlights the convergence of errors and covariance bounds with increasing steps, demonstrating improved estimation confidence.

represents the nonlinear simulation as already shown in Figures 1 and 2 , the blue points indicate the estimated projection, and time is shown with an arrow under the letter t. The right plots of each row display the residual errors (ΔP_x vs ΔP_y) for each feature after filtering.

Comparing with Figures 1 and 2, the blue trajectories demonstrate the significant improvement in precision achieved through filtering, as it closely follows the nonlinear simulation in red.

The residual errors further highlight the effectiveness of the filter. The green error distributions are tightly clustered around the origin, demonstrating the filter's ability to reject noise and produce accurate feature projections. These results underscore the importance of incorporating flexibility and noise rejection in the navigation filter to improve pose estimation and overall system precision.

CONCLUSION

In this study, a comprehensive framework for spacecraft navigation filtering in the presence of flexible dynamics was developed and validated. The challenges associated with flexibility, sloshing, and system uncertainties were addressed through an integrated approach, combining multibody modeling techniques with an LFR-based Kalman Filter.

In the multibody modeling section, the dynamics of a flexible spacecraft with appendages such as solar panels, boom antenna, and a robotic arm were modeled using the LFR formalism. This approach allowed the uncertainties in the system's dynamics to be efficiently encapsulated, enabling accurate representations of

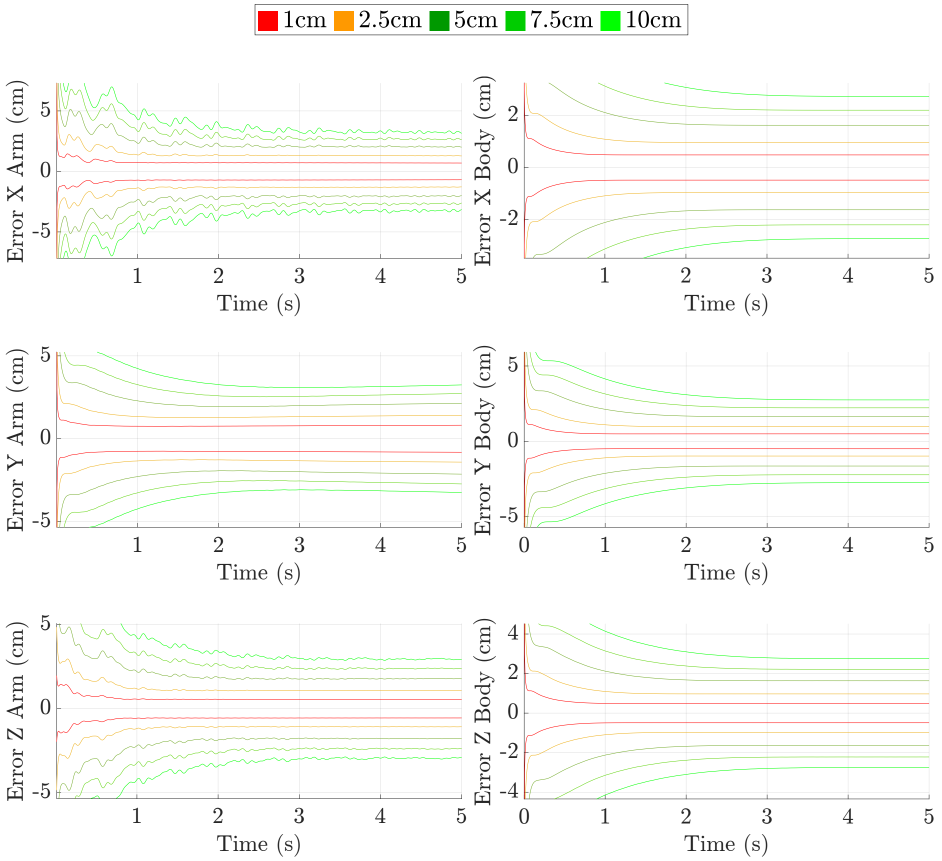

Figure 14. Position errors and 3σ covariance bounds with varying measurement noise levels (in meters). The figure highlights the impact of increasing measurement noise on covariance bounds and demonstrates the filter's robustness in maintaining errors within bounds.

the spacecraft's flexible behavior. The model was further validated using Simscape Multibody simulations, confirming its accuracy across a wide range of possible configurations.

The Navigation Filtering section detailed the development of an LFR-based Kalman Filter to update the linearized model in real-time based on the measurements. The filter's ability to integrate measurements from two distinct cameras (one on the rigid hub and another on the robotic arm's end-effector) was demonstrated. By accounting for the flexibility and couplings within the system, precise pose estimation was achieved, as verified through extensive simulations. The sensitivity of the navigation filter to various parameters, including measurement noise levels and correction time was investigated. The results showed the evolution of the 3σ covariance bounds across different scenarios. The importance of accurate noise modeling and sufficient correction time for achieving reliable state estimation was underscored.

The proposed framework has demonstrated its capability to enhance the precision and robustness of spacecraft navigation in scenarios involving significant flexibility and dynamic interactions. These results highlight its potential to be integrated into future mission designs, ensuring reliable performance even in challenging operational environments.

ACKNOWLEDGMENT

This paper is part of a Ph.D. work in progress at ISAE-SUPAERO, funded by the IRT (Technological Research Institute) of Saint-Exupéry, within the context of the RAPTOR project (Robotic and Artificial In-

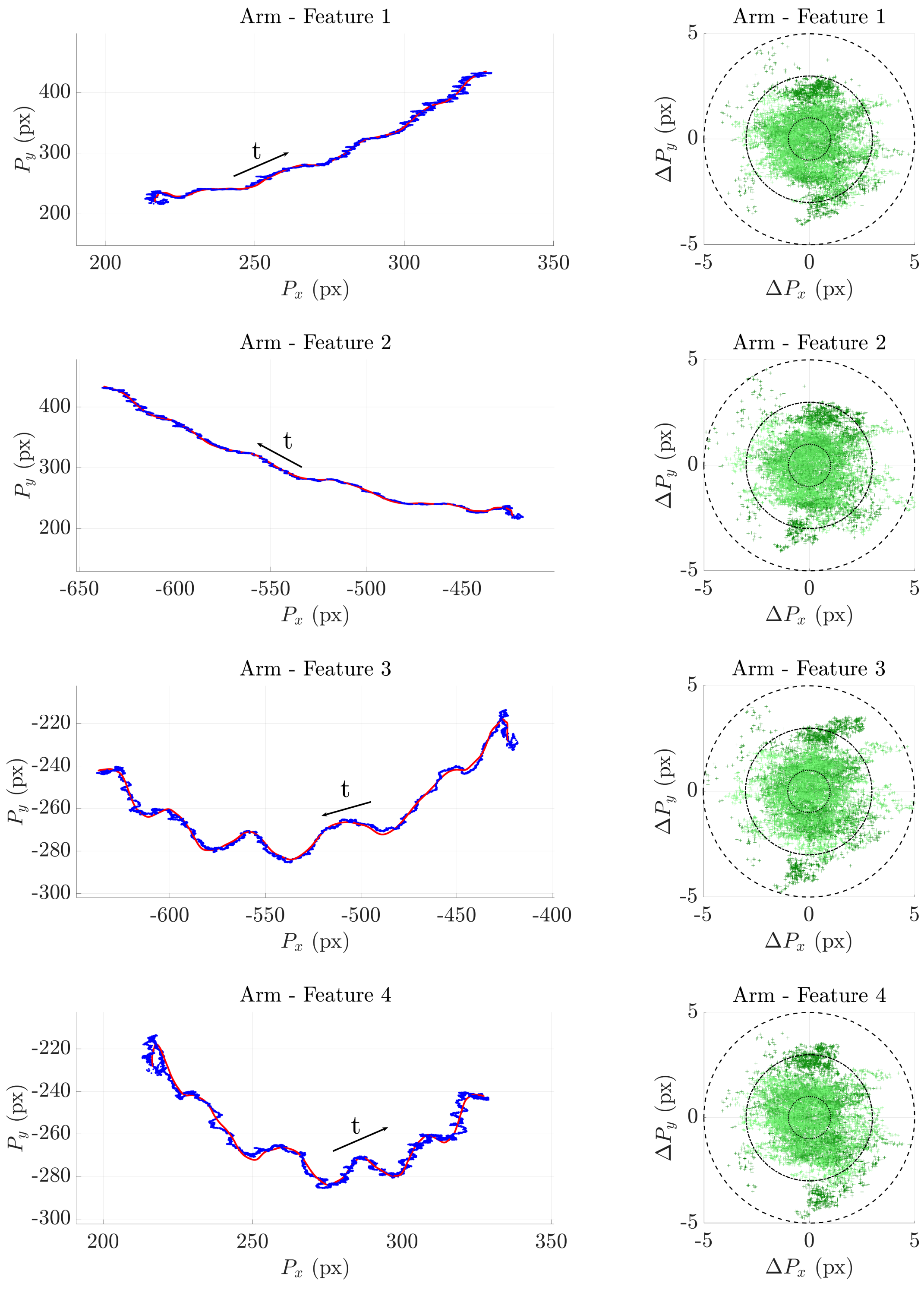

Figure 15. Projection of the features on the arm camera. The center of the image corresponds to $(0, 0)$ coordinates. The left column shows the feature projection trajectories, with red representing the nonlinear trajectories and blue representing the filtered ones. The right column shows the residual errors (ΔP_x vs ΔP_y) for each feature after filtering, highlighting the improved precision with respect to the quantitative study.

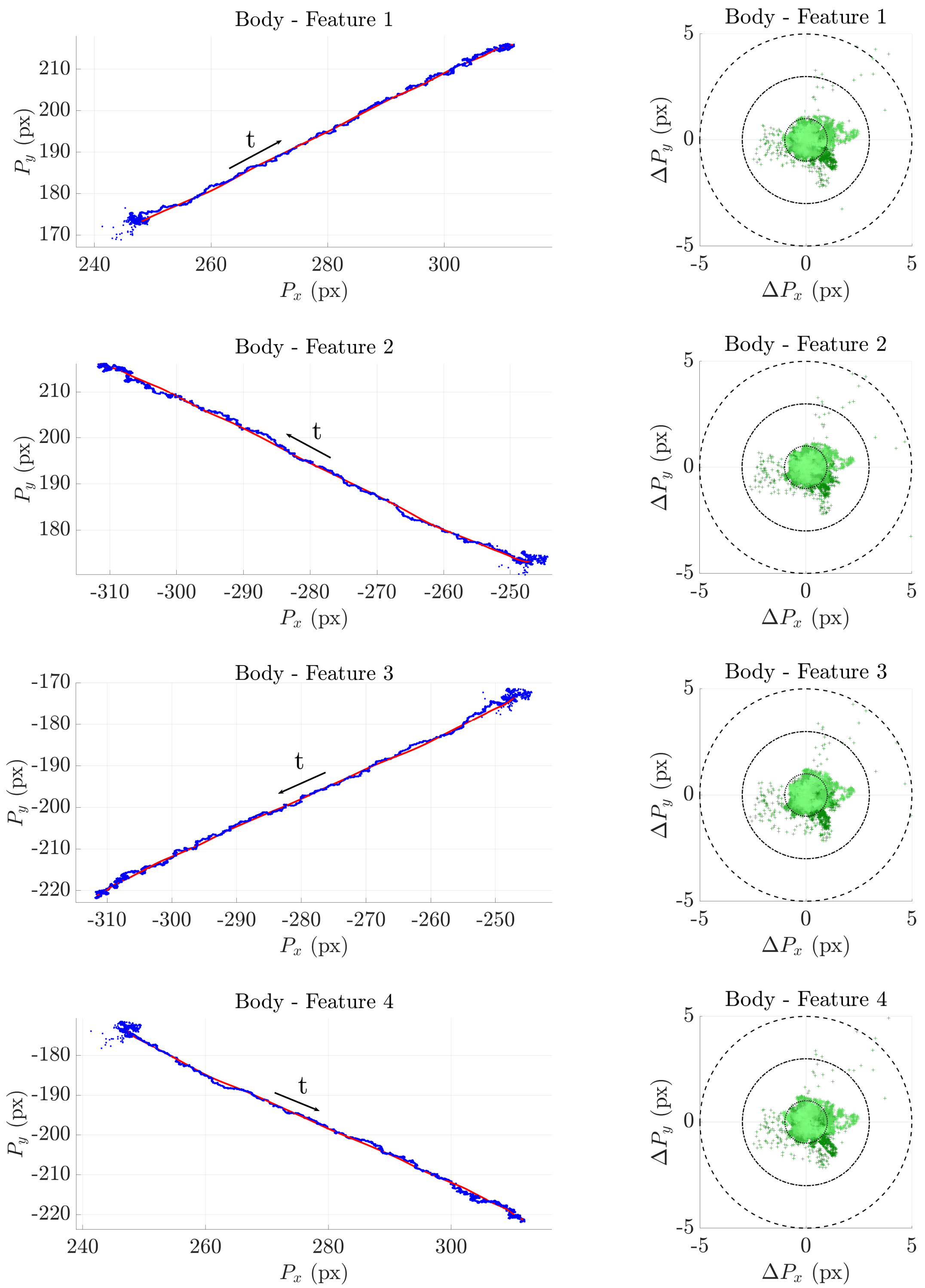

Figure 16. Projection of the features on the rigid body camera. The center of the image corresponds to $(0, 0)$ coordinates. The left column shows the feature projection trajectories, with red representing the nonlinear trajectories and blue representing the filtered ones. The right column shows the residual errors (ΔP_x vs ΔP_y) for each feature after filtering, highlighting the improved precision with respect to the quantitative study.

telligence Processing Test on Representative Target) for satellite rendezvous missions, in collaboration with Thales Alenia Space.

The navigation aspects of this work were conducted during a visiting period within the DART Lab at the Politecnico di Milano, whose valuable collaboration and technical support have greatly enriched the development and validation of this research.

REFERENCES

[1] W.-J. Li, D.-Y. Cheng, X.-G. Liu, Y.-B. Wang, W.-H. Shi, Z.-X. Tang, F. Gao, F.-M. Zeng, H.-Y. Chai, W.-B. Luo, *et al.*, “On-orbit service (OOS) of spacecraft: A review of engineering developments,” *Progress in Aerospace Sciences*, Vol. 108, 2019, pp. 32–120.

[2] F. Basana, Z. Pavanello, F. Branz, A. Francesconi, G. Borelli, D. Invernizzi, M. Massari, M. Lovera, A. Nocerino, R. Opromolla, *et al.*, “Satellite and robotic arm combined control for spacecraft close-proximity operations,” *CEAS Space Journal*, 2024, pp. 1–27.

[3] E. Papadopoulos, F. Aghili, O. Ma, and R. Lampariello, “Robotic manipulation and capture in space: A survey,” *Frontiers in Robotics and AI*, Vol. 8, 2021, p. 686723.

[4] X. Li, B. Duan, L. Song, Y. Yang, Y. Zhang, and D. Wang, “A new concept of space solar power satellite,” *Acta Astronautica*, Vol. 136, 2017, pp. 182–189.

[5] J. W. McMahon, H. K. Sipowa, M. Givens, and J. Cuberovic, “Soft-Robotic, Propellant-Free Servicers for LEO Spacecraft,” *2022 IEEE Aerospace Conference (AERO)*, IEEE, 2022, pp. 1–15.

[6] J. McMahon, S. K. Mitchell, K. Oguri, N. Kellaris, D. Kuettel, C. Keplinger, and B. Bercovici, “Area-of-effect softbots (aoes) for asteroid proximity operations,” *2019 IEEE Aerospace Conference*, IEEE, 2019, pp. 1–16.

[7] N. Faraco, M. Maestrini, M. Massari, P. Di Lizia, *et al.*, “Multiview Optical Navigation for Space Manipulator Systems During In-Orbit Servicing Missions,” *2024 AAS/AIAA Astrodynamics Specialist Conference*, 2024, pp. 1–16.

[8] D. Alazard, J. A. Perez, C. Cumer, and T. Loquen, “Two-input two-output port model for mechanical systems,” *Aiaa guidance, navigation, and control conference*, 2015, p. 1778.

[9] R. Rodrigues, F. Sanfedino, and D. Alazard, “Linear Parameter-Varying gain-scheduled attitude controller for a spinning spacecraft involving large flexible booms,”

[10] D. Alazard and F. Sanfedino, “Satellite dynamics toolbox library (sdtlib)-user’s guide,” 2021.

[11] R. Rodrigues, V. Preda, F. Sanfedino, and D. Alazard, “Modeling, robust control synthesis and worst-case analysis for an on-orbit servicing mission with large flexible spacecraft,” *Aerospace Science and Technology*, Vol. 129, 2022, p. 107865.

[12] F. Sanfedino, P. Iannelli, D. Alazard, E. Pelletier, S. Bennani, and B. Girouart, “European Satellite Benchmark for Control Education and Industrial Training,” *IFAC-PapersOnLine*, Vol. 58, No. 16, 2024, pp. 193–198. 2nd IFAC Workshop on Aerospace Control Education - WACE 2024, https://doi.org/10.1016/j.ifacol.2024.08.485.

[13] R. Rodrigues, F. Sanfedino, D. Alazard, V. Preda, and E. J. O. Delgado, “Linear parameter-varying gain-scheduled attitude controller for an on-orbit servicing mission involving flexible large spacecraft and fuel sloshing,” *ESA GNC AND ICATT 2023: 12th International Conference on Guidance, Navigation & Control Systems (GNC)*, 2023.

[14] U. Robots, “UR5 Robotic Arm,” `https://www.universal-robots.com/products/ur5-robot/`, 2024. Last Accessed: September 2024.

[15] K. Zhou and J. C. Doyle, *Essentials of robust control*, Vol. 104. Prentice hall Upper Saddle River, NJ, 1998.

[16] F. Sanfedino, D. Alazard, E. Kassarian, and F. Somers, “Satellite Dynamics Toolbox Library: a tool to model multi-body space systems for robust control synthesis and analysis,” *IFAC-PapersOnLine*, Vol. 56, No. 2, 2023, pp. 9153–9160.

[17] V. Dubanchet, *Modélisation et contrôle d’un robot spatial flexible pour la capture d’un débris en rotation*. PhD thesis, Toulouse, ISAE, 2016.

[18] H. Schaub and J. L. Junkins, *Analytical mechanics of space systems*. Aiaa, 2003.